

# Design and performance of a dual-laser instrument for multiple isotopologues of carbon dioxide and water

J. Barry McManus,\* David D. Nelson and Mark S. Zahniser

Aerodyne Research, Inc., 45 Manning Road, Billerica, MA 01821, USA

\* [mcmamus@aerodyne.com](mailto:mcmamus@aerodyne.com)

**Abstract:** A design and results for an instrument with a quantum cascade laser and an antimonide diode laser to measure simultaneously and with high precision seven isotopologues of carbon dioxide and water vapor. Methods and results for determining the effects that limit absorption noise at the level of  $5 \times 10^{-6}$  are presented and discussed.

©2015 Optical Society of America

**OCIS codes:** (280.3420) Laser sensors; (010.1280) Atmospheric composition; (300.6340) Spectroscopy, infrared; (140.5965) Semiconductor lasers, quantum cascade.

---

## References and links

1. J. Faist, *Quantum Cascade Lasers*, (Oxford University, 2013).
2. F. Capasso, C. Gmachl, R. Paiella, A. Tredicucci, A. L. Hutchinson, D. L. Sivco, J. N. Baillargeon, A. Y. Cho, and H. C. Liu, "New frontiers in quantum cascade lasers and applications," *IEEE J. Sel. Top. Quantum Electron.* **6**(6), 931–947 (2000).
3. C. Gmachl, F. Capasso, D. L. Sivco, and A. Y. Cho, "Recent progress in quantum cascade lasers and applications," *Rep. Prog. Phys.* **64**(11), 1533–1601 (2001).
4. M. Beck, D. Hofstetter, T. Aellen, J. Faist, U. Oesterle, M. Illegems, E. Gini, and H. Melchior, "Continuous wave operation of a mid-infrared semiconductor laser at room temperature," *Science* **295**(5553), 301–305 (2002).
5. Alpes Laser [Neuchatel, Switzerland, [www.alpeslasers.ch](http://www.alpeslasers.ch)]
6. I. Vurgaftman, W. W. Bewley, C. L. Canedy, C. S. Kim, M. Kim, J. R. Lindle, C. D. Merritt, J. Abell, and J. R. Meyer, "Mid-IR type-II interband cascade lasers," *IEEE J. Sel. Top. Quantum Electron.* **17**(5), 1435–1444 (2011).
7. C. L. Canedy, W. W. Bewley, J. R. Lindle, J. A. Nolde, D. C. Larrabee, C. S. Kim, M. Kim, I. Vurgaftman, and J. R. Meyer, "Interband cascade lasers with wavelengths spanning 2.9  $\mu\text{m}$  to 5.2  $\mu\text{m}$ ," *J. Electron. Mater.* **37**(12), 1780–1785 (2008).
8. Nanoplus, [www.nanoplus.com](http://www.nanoplus.com)
9. R. F. Curl, F. Capasso, C. Gmachl, A. A. Kosterev, B. McManus, R. Lewicki, M. Pusharsky, G. Wysocki, and F. K. Tittel, "Quantum cascade lasers in chemical physics," *Chem. Phys. Lett.* **487**(1-3), 1–18 (2010).
10. F. K. Tittel, Y. Bakhrkin, A. A. Kosterev, and G. Wysocki, "Recent advances in trace gas detection using quantum and interband cascade lasers," *Rev. Laser Eng.* **34**(4), 275–282 (2006).
11. F. K. Tittel, D. Richter, and A. Fried, "Mid-infrared laser applications in spectroscopy," *Topics in Appl. Phys.* **89**, 445–516, I. T. Sorokina, and K. L. Vodopyanov, Eds., (Springer-Verlag, 2003).
12. C. Dyroff, D. Fütterer, and A. Zahn, "Compact diode-laser spectrometer ISOWAT for highly sensitive airborne measurements of water-isotope ratios," *Appl. Phys. B* **98**(2-3), 537–548 (2010).
13. G. Wysocki, A. A. Kosterev, and F. K. Tittel, "Spectroscopic trace-gas sensor with rapidly scanned wavelengths of a pulsed quantum cascade laser for *in situ* NO monitoring of industrial exhaust systems," *Appl. Phys. B* **80**(4-5), 617–625 (2005).
14. G. Hancock, G. Ritchie, J.-P. von Helden, R. Walker, and D. Weidmann, "Applications of midinfrared quantum cascade lasers to spectroscopy," *Opt. Eng.* **49**(11), 111121 (2010).
15. E. Kerstel and L. Gianfrani, "Advances in laser-based isotope ratio measurements: selected applications," *Appl. Phys. B* **92**(3), 439–449 (2008).
16. V. Spagnolo, A. A. Kosterev, L. Dong, R. Lewicki, and F. K. Tittel, "NO trace gas sensor based on quartz-enhanced photoacoustic spectroscopy and external cavity quantum cascade laser," *Appl. Phys. B* **100**(1), 125–130 (2010).
17. S. Viciani, F. D'Amato, P. Mazzinghi, G. Toci, and P. Werle, "A cryogenically operated laser diode spectrometer for airborne measurement of stratospheric trace gases," *Appl. Phys. B* **90**(3-4), 581–592 (2008).
18. C. R. Webster, G. J. Flesch, D. C. Scott, J. E. Swanson, R. D. May, W. S. Woodward, C. Gmachl, F. Capasso, D. L. Sivco, J. N. Baillargeon, A. L. Hutchinson, and A. Y. Cho, "Quantum-cascade laser measurements of stratospheric methane and nitrous oxide," *Appl. Opt.* **40**(3), 321–326 (2001).

19. J. Jágerská, B. Tuzson, H. Looser, A. Bismuto, J. Faist, H. Prinz, and L. Emmenegger, "Highly sensitive and fast detection of propane-butane using a 3  $\mu\text{m}$  quantum cascade laser," *Appl. Opt.* **52**(19), 4613–4619 (2013).
20. B. Tuzson, J. Mohn, M. J. Zeeman, R. A. Werner, W. Eugster, M. S. Zahniser, D. D. Nelson, J. B. McManus, and L. Emmenegger, "High precision and continuous field measurements of  $\delta^{13}\text{C}$  and  $\delta^{18}\text{O}$  in carbon dioxide with a cryogen-free QCLAS," *Appl. Phys. B* **92**(3), 451–458 (2008).
21. Aerodyne Research, Inc., [www.aerodyne.com](http://www.aerodyne.com)
22. Los Gatos Research, [www.lgrinc.com](http://www.lgrinc.com)
23. J. B. McManus, M. S. Zahniser, and D. D. Nelson, "Dual quantum cascade laser trace gas instrument with astigmatic Herriott cell at high pass number," *Appl. Opt.* **50**(4), A74–A85 (2011).
24. J. B. McManus, M. S. Zahniser, D. D. Nelson, J. H. Shorter, S. C. Herndon, E. Wood, and R. Wehr, "Application of quantum cascade lasers to high-precision atmospheric trace gas measurements," *Opt. Eng.* **49**(11), 111124 (2010).
25. J. B. McManus, D. D. Nelson, and M. S. Zahniser, "Long-term continuous sampling of  $^{12}\text{CO}_2$ ,  $^{13}\text{CO}_2$  and  $^{12}\text{C}^{18}\text{O}^{16}\text{O}$  in ambient air with a quantum cascade laser spectrometer," *Isotopes Environ. Health Stud.* **46**(1), 49–63 (2010).
26. D. D. Nelson, J. B. McManus, S. C. Herndon, M. S. Zahniser, B. Tuzson, and L. Emmenegger, "New method for isotopic ratio measurements of atmospheric carbon dioxide using a 4.3  $\mu\text{m}$  pulsed quantum cascade laser," *Appl. Phys. B* **90**(2), 301–309 (2008).
27. J. B. McManus, D. D. Nelson, S. C. Herndon, J. H. Shorter, M. S. Zahniser, S. Blaser, L. Hvozدارa, A. Muller, M. Giovannini, and J. Faist, "Comparison of CW and Pulsed Operation with a TE-Cooled Quantum Cascade Infrared Laser for Detection of Nitric Oxide at 1900  $\text{cm}^{-1}$ ," *Appl. Phys. B* **28**, 235–241 (2006).
28. D. D. Nelson, J. B. McManus, S. C. Herndon, J. H. Shorter, M. S. Zahniser, S. Blaser, L. Hvozدارa, A. Muller, M. Giovannini, and J. Faist, "Characterization of a near-room-temperature, continuous-wave quantum cascade laser for long-term, unattended monitoring of nitric oxide in the atmosphere," *Opt. Lett.* **31**(13), 2012–2014 (2006).
29. D. D. Nelson, J. H. Shorter, J. B. McManus, and M. S. Zahniser, "Sub-part-per-billion detection of nitric oxide in air using a thermoelectrically cooled mid-infrared quantum cascade laser spectrometer," *Appl. Phys. B* **75**(2-3), 343–350 (2002).
30. R. Q. Iannone, S. Kassi, H.-J. Jost, M. Chenevier, D. Romanini, H. A. J. Meijer, S. Dhanyiala, M. Snels, and E. R. T. Kerstel, "Development and airborne operation of a compact water isotope ratio infrared spectrometer," *Isotopes Environ. Health Stud.* **45**(4), 303–320 (2009).
31. P. Werle, "A review of recent advances in semiconductor laser based gas monitors," *Spectrochimica Acta Part A* **54**(2), 197–236 (1998).
32. L. S. Rothman, I. E. Gordon, Y. Babikov, A. Barbe, D. Chris Benner, P. F. Bernath, M. Birk, L. Bizzocchi, V. Boudon, L. R. Brown, A. Camparguej, K. Chance, E. A. Cohen, L. H. Coudert, V. M. Devi, B. J. Drouin, A. Fayt, J.-M. Flaud, R. R. Gamache, J. J. Harrison, J.-M. Hartmann, C. Hill, J. T. Hodges, D. Jacquemart, A. Jolly, J. Lamouroux, R. J. Le Roy, G. Li, D. A. Long, O. M. Lyulin, C. J. Mackie, S. T. Massie, S. Mikhailenko, H. S. P. Müller, O. V. Naumenko, A. V. Nikitin, J. Orphal, V. Perevalov, A. Perrin, E. R. Polovtseva, C. Richard, M. A. H. Smith, E. Starikova, K. Sung, S. Tashkun, J. Tennyson, G. C. Toon, V. G. Tyuterev, and G. Wagner, "The HITRAN2012 molecular spectroscopic database," *JQSRT* **130**, 4–50 (2013).
33. J. B. McManus, "Paraxial matrix description of astigmatic and cylindrical mirror resonators with twisted axes for laser spectroscopy," *Appl. Opt.* **46**(4), 472–482 (2007).
34. J. B. McManus, P. L. Kebabian, and M. S. Zahniser, "Astigmatic mirror multipass absorption cells for long-path-length spectroscopy," *Appl. Opt.* **34**(18), 3336–3348 (1995).
35. A. Vicet, D. A. Yarekha, A. Pérona, Y. Rouillard, S. Gaillard, and A. N. Baranov, "Trace gas detection with antimonide-based quantum-well diode lasers," *Spectrochim. Acta A Mol. Biomol. Spectrosc.* **58**(11), 2405–2412 (2002).
36. P. Werle, R. Mucke, and F. Slemr, "The limits of signal averaging in atmospheric trace-gas monitoring by tunable diode-laser absorption spectroscopy (TDLAS)," *Appl. Phys. B* **57**, 131–139 (1993).
37. R. Wehr, J. W. Munger, D. D. Nelson, J. B. McManus, M. S. Zahniser, S. C. Wofsy, and S. R. Saleska, "Measuring forest-atmosphere exchange of  $^{13}\text{C}^{16}\text{O}_2$ ,  $^{18}\text{O}^{12}\text{C}^{16}\text{O}$ , and  $^{12}\text{C}^{16}\text{O}_2$  by eddy covariance," *Agric. For. Meteorol.* **181**, 69–84 (2013).
38. P. Sturm, W. Eugster, and A. Knohl, "Eddy covariance measurements of  $\text{CO}_2$  isotopologues with a quantum cascade laser absorption spectrometer," *Agric. For. Meteorol.* **152**, 73–82 (2012).
39. R. Wehr, J. W. Munger, D. D. Nelson, J. B. McManus, M. S. Zahniser, S. C. Wofsy, and S. R. Saleska, "Long-term eddy covariance measurements of the isotopic composition of the ecosystem–atmosphere exchange of  $\text{CO}_2$  in a temperate forest," *Agric. For. Meteorol.* **181**, 69–84 (2013).
40. J. B. McManus, M. S. Zahniser, D. D. Nelson, J. H. Shorter, S. C. Herndon, D. Jervis, M. Agnese, R. McGovern, T. I. Yacovitch, and J. R. Roscioli, "Recent progress in laser based trace gas instruments: performance and noise analysis," *Appl. Phys. B10.1007/s00340-015-6033-0* (2015).

## 1. Introduction

With the maturation of mid infrared semiconductor lasers based on quantum engineering, i.e. the quantum cascade laser (QCL) [1–5] and the interband cascade laser (ICL) [6–8], designers

of instruments to measure gases in trace amounts enjoy full access to the wavelengths where those measurements can be made with the greatest sensitivity. Many small molecules have their strongest absorption lines in the spectral region between  $\sim 3$  and  $10\ \mu\text{m}$ , the spectral region spanned by QCL's and ICL's. Trace gas instruments utilizing these mid-IR lasers are being designed at universities [9–17], government laboratories [18–20] and in corporations [21–29], in order to help answer pressing questions in atmospheric and environmental research. QCL's and ICL's are nearly ideal sources for trace gas instruments that must operate outside the laboratory, since they can operate at near room temperature, they are small and robust, and can be easily modulated in wavelength. In this paper we present more detailed results from a new instrument that has two laser sources, a QCL and a TDL, in order to measure simultaneously seven isotopologues of carbon dioxide and water vapor.

The Center for Atmospheric and Environmental Chemistry at Aerodyne Research, Inc. (ARI) has produced more than 120 laser-based atmospheric trace gas instruments over the last 10 years, to measure more than 25 different gases or isotopologues of gases, with sensitivities in some cases reaching sub parts per trillion. The absorption noise for the best of these results is on the order of  $\sim 5 \times 10^{-6}$  in 1 s. Over the course of development, building and testing instruments over the last  $\sim 5$  years we have evaluated and used more than 300 (combined) QCL's and ICL's in this very demanding application. Most of our instrument lasers are QCL's from Alpes Laser [5]. Alpes Laser was the first company to provide QCL's at the specific wavelengths best suited to measuring a variety of trace gases. While the first commercially available mid-IR QCL's were pulsed, now we use CW lasers almost exclusively. CW-QCL's give better results in instruments due to higher power, narrower linewidth and better stability [27, 28]. Recently, ICL's operating near  $3\ \mu\text{m}$  have become commercially available [8] and help fill in the availability of laser wavelengths near the C-H stretch absorption bands of many hydrocarbon compounds. We have found that in most cases these CW QCL's and ICL's are nearly ideal laser sources, and without them our high-precision instruments would not be possible.

In this paper we present a dual laser instrument that combines a  $4.3\ \mu\text{m}$  QCL and a  $2.773\ \mu\text{m}$  TDL to simultaneously measure four isotopologues (isotopic variants) of  $\text{CO}_2$  and three isotopologues of water vapor at ambient concentrations and with high precision. This is a very demanding application of laser technology, and these two types of lasers work together seamlessly. Isotopologues with relatively deep absorption lines are measured with a precision of  $\sim 0.1\%$  (one part in  $10^4$ ) in 1 s. We will review our general design strategy, and the specific design of a two-laser instrument for isotopologues of carbon dioxide and water vapor. We will describe the characteristics of the measurement noise for seven isotopologues and the application of a calibration system. We will discuss a detailed analysis of the limiting noise effects.

A note on isotopic terminology may be useful at this point, since we use this language in the description of our instrument performance. An isotope of an atom is just an indication of the number of neutrons in the nucleus, reported in terms of the total atomic mass (written as left superscript). In most cases there is a “major isotope” that accounts for the great majority of the atoms found in nature, and one or more “minor isotopes” that are relatively rare. For example: natural carbon is 98.9%  $^{12}\text{C}$  and 1.1%  $^{13}\text{C}$ ; oxygen is 99.759%  $^{16}\text{O}$ , 0.204%  $^{18}\text{O}$  and 0.037%  $^{17}\text{O}$ ; and hydrogen is 99.985%  $^1\text{H}$  and 0.015%  $^2\text{H}$ , ( $^2\text{H}$  is sometimes written D for deuterium). “Isotopologues” are molecules where a minor isotope atom substitutes for a major isotope. There may be zero, one or more substitutions. Where the site of substitution in the molecule is important, we distinguish “isotopomers”. Various physical and chemical processes slightly alter the mixture of minor and major isotopologues, and thus changes in the isotopic ratio in a sample may carry evidence of its history. The minor isotope changes of interest are typically small, perhaps 0.1 to 10 parts per thousand (per mil, ‰). Thus the required measurement precision is quite a challenge, as one needs to measure changes of

$\sim 10^{-4}$  in the minor isotope ( $< \sim 1\%$  of the total) of a gas that may be a small fraction of the atmosphere.

## 2. General approaches in trace gas instrument designs at Aerodyne Research, Inc

The general approach to trace gas laser instruments at Aerodyne Research, Inc. (ARI) is direct absorption spectroscopy in the mid-infrared with fast frequency sweeps and precision spectral fitting. A multi-pass absorption cell provides enough path length that the absorption depth is sufficient for accurate measurements, optimally with optical depth between 0.1 and 1. For strongly absorbing gases at high concentrations, a few centimeters of path may be sufficient; other measurement problems require a path-length of hundreds of meters. The multi-pass cell has a definite path length, and a good fraction of the laser light may be transmitted to the detector, minimizing the effects of detector noise.

To measure an absorption line, we rapidly scan (at  $\sim 1$ -3 kHz) the laser frequency over the absorption line and a section of low-absorption baseline to either side of the line, and then reduce the laser current to below threshold on each sweep to measure the signal at zero light output. The detected laser sweeps are averaged and then fit with combination of laser intensity baseline forms and absorption line shapes, typically a Voigt function. The Voigt profile is calculated based on measured quantities and the absorption length is known, so the mixing ratio can be quantitatively determined.

The operating software, "TDLWintel", is set up to run a single laser or to time-multiplex two lasers. The basic operation of the software has been described in a previous publication [29], but we repeat some of the essential characteristics for completeness here. TDLWintel both controls the operation of the spectrometer and processes the data in real time. The laser current ramps for both lasers are defined by TDLWintel and then detected signals are synchronously averaged and then fit with calculated absorption profiles based on HITRAN parameters [32] and measured temperature and pressure. Calculated mixing ratios for up to 16 gases are recorded in real time, and averaged spectra are archived. Data may be recorded at up to 10 Hz, but the maximum useful data rate is set by the pumping speed and the size of the absorption cell. Experimental events, such as valve openings or background subtractions, also may be controlled by TDLWintel. A feedback system using the measured absorption line center actively controls the laser base temperature, so that average line positions can be maintained with a stability of  $\sim 2 \times 10^{-4} \text{ cm}^{-1}$ .

We have enjoyed a significant improvement in the performance of our instruments over the last five years, with much of the improvement due to reduced noise power supplies and laser drivers. The instrument employs a QC laser current driver manufactured by Wavelength Electronics ([www.teamwavelength.com](http://www.teamwavelength.com)) designed to provide low noise current at the high compliance voltage typical of QCL's. The laser current driver and other electronics are powered by low-noise supplies of our own design. Efforts to reduce electronic noise throughout the system have resulted in exceptional performance. Our standard of good performance is to measure with an absorption noise of  $\sim 5 \times 10^{-6}$  with 1s average. A well-performing instrument should have improved precision with longer averaging, out to  $\sim 100$  s averaging. That corresponds to an ultimate absorption noise of  $\sim 5 \times 10^{-7}$ . The short term noise is typically 2 to 6 times greater than the detector noise. There are numerous effects that can increase the noise above the detector's limit, especially narrowband electronic noise and optical fringes.

## 3. Design of dual laser instrument for multiple isotopologues of carbon dioxide and water

We have recently built a version of our two-laser instrument platform for high precision simultaneous measurements of multiple isotopologues of carbon dioxide and water vapor. The motivation for the design of the instrument to measure multiple isotopologues of carbon dioxide and water is to provide more information on the sources and sinks of  $\text{CO}_2$  in the

atmosphere. The increase of carbon dioxide in the Earth's atmosphere is the most important driver of global warming. In order to predict future carbon dioxide concentrations under various mitigation strategies, we require much better quantitative understanding of the sources and sinks of atmospheric carbon dioxide. Studying the ratios of the stable isotopes of carbon dioxide has long been recognized as a tool for identifying sources and sinks of atmospheric carbon dioxide. Because of the coupling of the water and carbon dioxide cycles (through oxygen exchange), measurements of isotopic water vapor are also required to quantify the carbon cycle. In particular, simultaneous measurement of fluxes of  $^{12}\text{C}^{18}\text{O}^{16}\text{O}$  and  $\text{H}_2^{18}\text{O}$  may allow partitioning of fluxes between plant photosynthesis and respiration [15, 37–39]. Wider use of stable isotopes in ecosystem exchange studies has been impeded by the difficulty of making these measurements at the requisite precision (better than 0.2 ‰) and by the complication that existing instrumentation using isotope ratio mass spectrometry (IRMS) requires samples to be collected in flasks and returned to the laboratory for analysis. A fast (10 Hz), high precision monitor for the stable isotopologues of carbon dioxide and water could find use in the atmospheric measurements community.

### 3.1 Spectroscopic choices

Adapting our dual laser instrument platform to the problem of measuring multiple isotopologues of carbon dioxide and water begins with the choice of absorption lines, with two main considerations: the lines must be closely spaced ( $< 0.5$  to  $1\text{ cm}^{-1}$ ) so that they fall within the current-scan range of the laser; and the lines should be free of interference by other absorption lines from other gases. Additional preferences are to have lines that are of nearly equal strength, and that the temperature dependence of the line strengths should be low. The set of lines for  $\text{CO}_2$  at  $2310\text{ cm}^{-1}$  are exceptional in these regards [15, 20, 26]. Water is a more difficult case, because of the much lower natural abundance of deuterated water (fraction  $\text{HDO}/\text{H}_2\text{O} \sim 3 \times 10^{-4}$ ), especially compared to the  $^{18}\text{O}$  isotopologue (fraction  $^1\text{H}_2^{18}\text{O}/\text{H}_2\text{O} \sim 2.5 \times 10^{-3}$ ). We surveyed possible wavelength regions that have water absorption lines and are within the tuning range of commercially available antimonide diode lasers. We survey the spectral regions using software that simulates the total absorption for all of the common atmospheric gases at nominal ambient concentrations, using HITRAN [32] spectroscopic parameters. Pressure, temperature and path length are based on reasonable choices for the planned instrument. In the end, we chose to use the same spectral line as C. Dyroff [12], at  $3765\text{ cm}^{-1}$ . These are a well-studied set of lines that are relatively free of interferences [12, 15, 30]. There are some very weak  $\text{CO}_2$  and  $\text{N}_2\text{O}$  lines near the  $\text{H}_2\text{O}$  lines, but those can be accounted for in multi-species fitting. A disadvantage of these lines is that the HDO line is very weak, and is close to a strong  $\text{H}_2\text{O}$  line which may interfere.

The completed instrument employs a combination of two laser technologies, in which carbon dioxide isotopologues are measured with a  $4.3\text{ }\mu\text{m}$  quantum cascade and water vapor isotopologues are measured with an antimonide-based  $2.77\text{ }\mu\text{m}$  diode laser [35]. The instrument embodies choices and compromises to give the best simultaneous measurement of seven isotopologues. For example, a longer path-length (36 m) than usual ( $\sim 7\text{ m}$ ) is used for the  $\text{CO}_2$  measurement in order to have sufficient path-length for the rare deuterium isotopologue of water.

### 3.2 Optical design

The optical design for the instrument is shown in Fig. 1. An earlier version of the two laser instrument has been presented [23], so the discussion here is brief. The optics are built on a  $43 \times 64\text{ cm}$  temperature-controlled table, with a cover that seals well enough to allow purging the optics with dry  $\text{CO}_2$ -free air. The optical path begins with the two lasers mounted on Peltier coolers in sealed housings. Laser light is collected by a pair of 15X reflecting objectives, then combined into a single beam with a wedged ZnSe plate and focused through

the same pinhole. The pinhole is only present during alignment, as it will generate strong interference fringes. Additional imaging optics transform the combined beam into the very narrow beam (F#100) that works best in the astigmatic Herriott cell [33, 34]. The cell may be selected according to the measurement problem, to provide absorption path length from 7 to 210 m. The output of the cell is focused onto a thermoelectrically cooled detector. The dual laser instrument has two reference paths, derived from reflection from the two faces of a wedged BaF<sub>2</sub> beamsplitter. There is a “Reference Locking” path that contains a short gas cell with high concentrations of the gases of interest. Fitting to absorption lines produced by the gas cell allows us to lock the laser frequencies to specific absorption lines, in case the sample gas contains too little of the gas of interest. The other reference path may be used for power normalization, or a Ge etalon may be flipped into the path in order to measure the laser tuning rates. An electromagnetically actuated flag may be flipped to allow either reference beam to reach the single reference detector.

There are several elements of the optical design that are intended to ease alignment, both when installing lasers and when optimizing coupling light into the multipass cell. A red laser is co-aligned with the infrared by focusing through the pinhole, so that we can visualize the path from the pinhole all the way to the detectors. Both IR beams reflect from visible-IR dichroics, which allows us to have viewing points for both lasers. A drop-in eyepiece placed behind a dichroic, combined with the 15X objective, creates a 150X microscope with which to view the laser face. When a laser is replaced, we can center it in the microscope field of view, which also approximately centers its image at the pinhole location. By directing a light source (e.g. LED) backwards through the pinhole, a visible image of the pinhole can be adjusted to be exactly on the laser viewed through the microscope. The sequence of images upstream and downstream of the pinhole are made to correspond, and the image of the laser is ultimately connected to the detector. In this way we can rapidly find the IR light on the detector and optimize transmission through the system. Another element of the design facilitates coupling into the multipass cell. A focusing mirror before the cell gives a final stage of beam magnification, but it also results in independent aiming adjustments for the multi-pass cell hole and the setting of the pattern size on the mirrors. The focusing mirror before the cell creates virtual images of the cell hole and back cell mirror on the two preceding aiming mirrors. Generally one is free to tilt a mirror with an image on it without changing the location of the following image. Thus, we tilt the mirror with the virtual image of the cell hole and the beam moves at the back of the cell, but not at the hole. Similarly, we tilt the other adjustment mirror and the beam moves at the coupling hole and not at the back of the cell. Tedious iterative adjustment of the mirrors aiming into the cell is avoided.

We have completed the construction and test of the prototype instrument for simultaneous measurement of abundances of four isotopologues of CO<sub>2</sub> (<sup>12</sup>C<sup>16</sup>O<sup>16</sup>O, <sup>12</sup>C<sup>17</sup>O<sup>16</sup>O, <sup>12</sup>C<sup>18</sup>O<sup>16</sup>O, <sup>13</sup>C<sup>16</sup>O<sup>16</sup>O), and three isotopologues of H<sub>2</sub>O (<sup>1</sup>H<sub>2</sub><sup>16</sup>O, <sup>1</sup>H<sub>2</sub><sup>18</sup>O, <sup>2</sup>H<sup>1</sup>H<sup>16</sup>O). The characteristics of the absorption lines are summarized in Table 1. A sample spectrum is shown in Fig. 2.

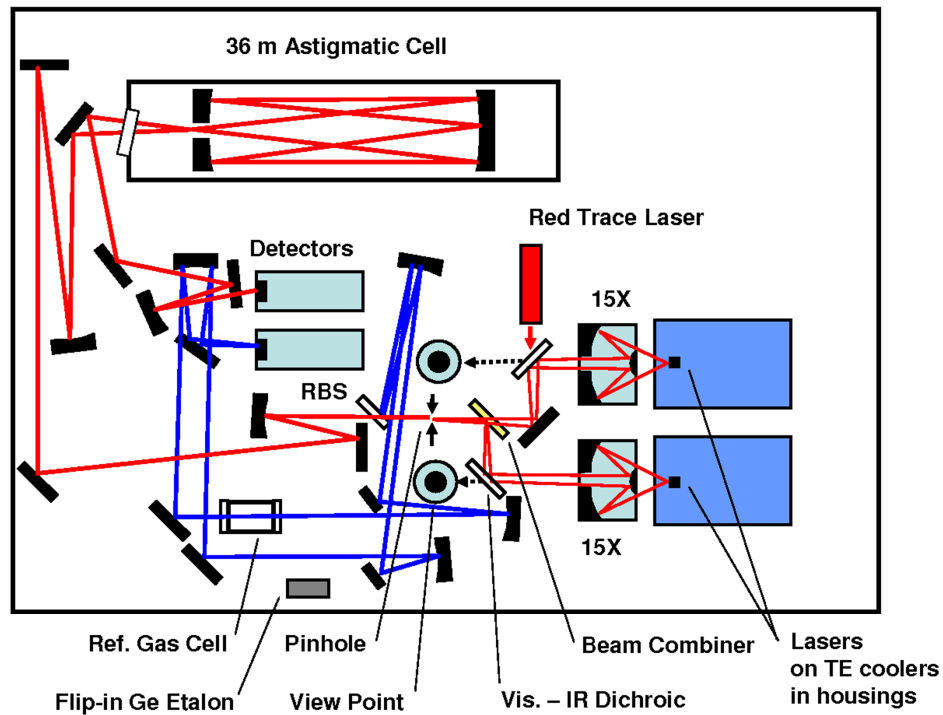


Fig. 1. Diagram of the optical layout for the dual laser instrument. The main sample measurement path is colored red, while the reference paths are shown in blue. The sample path includes a 36 m absorption cell. The two reference paths are derived by the reflections from both sides of a wedged BaF2 plate. One reference path contains a short reference gas cell and the other has an etalon that may be flipped into the beam for measurement of laser tuning rates. Both reference beams are focused on the same detector, with the choice of which is active made by flipping an opaque flag into one reference beam or the other.

Table 1. Ambient air absorption line characteristics, 30 Torr, 36 m

Isotopologue	freq, $\text{cm}^{-1}$	OD	Conc., ppb	OD/conc., $\text{ppb}^{-1}$
H <sub>2</sub> O	3764.599	2.35	$1.28 \times 10^7$	$1.84 \times 10^{-7}$
HDO	3764.876	0.039	$1.2 \times 10^7$	$3.25 \times 10^{-9}$
H <sub>2</sub> <sup>18</sup> O	3765.091	0.197	$1.2 \times 10^7$	$1.64 \times 10^{-8}$
CO <sub>2</sub>	2310.002	0.862	$5.3 \times 10^5$	$1.56 \times 10^{-6}$
C <sup>17</sup> O <sup>16</sup> O	2309.983	0.1	$5.1 \times 10^5$	$1.96 \times 10^{-7}$
C <sup>18</sup> O <sup>16</sup> O	2310.206	0.81	$5.1 \times 10^5$	$1.57 \times 10^{-6}$
<sup>13</sup> CO <sub>2</sub>	2310.347	1.17	$5.1 \times 10^5$	$2.2 \times 10^{-6}$

OD is optical depth ( $-\ln(\text{transmission})$ ).

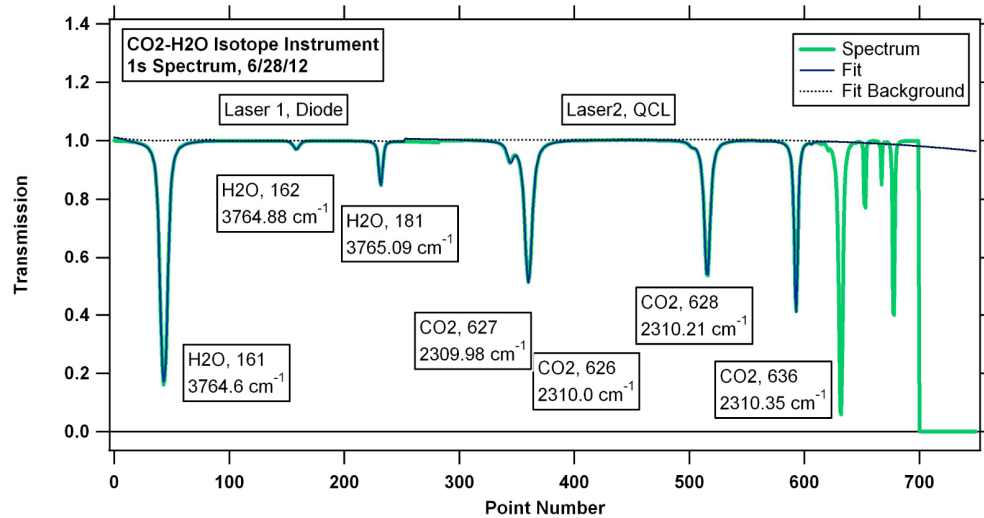


Fig. 2. Absorption spectrum for H<sub>2</sub>O and CO<sub>2</sub> obtained with the dual isotope instrument with water vapor and carbon dioxide at ambient levels and a 36 m absorption path in a pressure of ~30 Torr. The measured spectrum is the green trace, and the fit is the black trace. The fit background is the black dotted line.

### 3.3 Isotopologue calibration system

Isotopic measurements at high precision generally implies the need for a calibration system, i.e. a system for periodically injecting a reference gas with known isotopic composition. Precise isotopic composition of a trace gas must be related to a broadly accepted standard. Thus, the isotopic measurement of a sample is presented as a super-ratio,  $R$ , of a measured ratio of minor/major isotopologues for the sample, divided by a similarly measured ratio for a standard of known isotopic composition,

$$R = ([\text{minor isotope}] / [\text{major isotope}])_{\text{sample}} / ([\text{minor isotope}] / [\text{major isotope}])_{\text{standard}} .$$

Eq. (1)

The “known” standard may be a transfer standard, cross calibrated to a global standard. In a laser spectroscopic system, one must expect that there will be many sources of drift in the isotopic measurement, so that periodic re-measurement of a transfer standard will be crucial in maintaining isotopic measurement accuracy and precision. A typical calibration system employs several transfer standards at different concentrations and isotopic ratios, using a set of compressed air tanks and regulators.

A particular calibration concern in our dual isotope instrument is the large optical depth of the normal water and the CO<sub>2</sub> lines. Since we use a path length of 36 meters in order to increase the absorption depth for rare HDO, the more abundant isotopologues have deeper than optimal absorption lines. At typical ambient concentrations, the optical depth ( $\ln(\text{transmission})$ ) for the major isotopologue water line is ~1.5 to 2, and the optical depths for the CO<sub>2</sub> lines are ~1. That is in contrast to our usual choice of optical depths of 0.1 to 0.2. Making precise measurements of all the isotopologues will be an even greater challenge at above-ambient concentrations. Although the spectral fitting routines account for non-linear absorption at large optical depths, some residual nonlinearity of the instrument response is an expected result of these large optical depths, and the contrast in optical depths.

The design of a calibration system for both water and carbon dioxide isotopologues presents special challenges, in that one cannot have gaseous mixtures of water and CO<sub>2</sub> standards in compressed gas tanks. Rather, liquid water must be converted to vapor diluted in dry air, via a process that does not introduce unexpected isotopic fractionation. Since the

simple process of evaporation of liquid water does introduce fractionation, one should either ensure complete evaporation of small injections of water, or use a larger volume of water at a known temperature and use only a small amount so that the isotopic mix does not change. The flow rate from the calibration source should match that needed for the fastest measurements (e.g. for eddy flux measurements), i.e. a cell flush time of 0.1 s. With our 0.3 liter cell working at  $\sim 1/20$  atmosphere, the gas flow at atmospheric pressure is up to  $\sim 10$  liters/minute.

The prototype calibration system is a simple and compact system that is suitable for field measurement applications (Fig. 3). The system works by dynamic dilution of transfer standards at high concentration ( $\sim 100\%$ ) with “zero” air (dry,  $\text{CO}_2$  free), to present the instrument with gas of variable concentration but fixed isotopic composition. Sample measurements are divided by a calibration cycle derived response curve, giving a first isotopic super ratio that accounts for possible instrument nonlinearity. Since the reference materials are at high concentration, their consumption rate can be quite low.

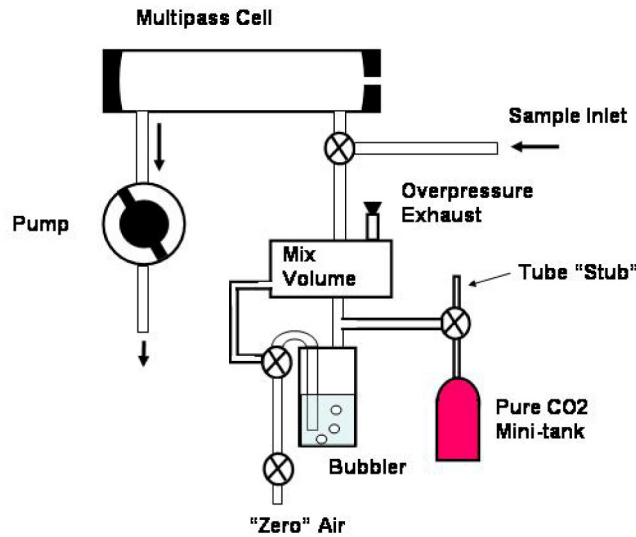


Fig. 3. Diagram of the water- $\text{CO}_2$  calibration system.

#### 4. Measurement results with the dual laser instrument

##### 4.1 Basic measurement noise

The basic instrument measurement noise performance is demonstrated with a set of Allan-Werle plots (variance as a function of averaging time) [37]. Allan-Werle plots of isotopic ratios for segments of data sampling ambient air are shown in Figs. 4-7, with the results summarized in Table 2.

Table 2. Dual Isotope Instrument Noise Performance, Ambient Air

Isotopologue Ratio	1s Noise, ‰	Variance Minimum Time, s	Variance Minimum Standard Deviation, ‰
HDO	0.3	33	0.07
$\text{H}_2^{18}\text{O}$	0.1	33	0.03
$\text{C}^{17}\text{O}^{16}\text{O}$	8.8	220	3.0
$\text{C}^{18}\text{O}^{16}\text{O}$	0.08	45	0.01
$^{13}\text{CO}_2$	0.13	43	0.02

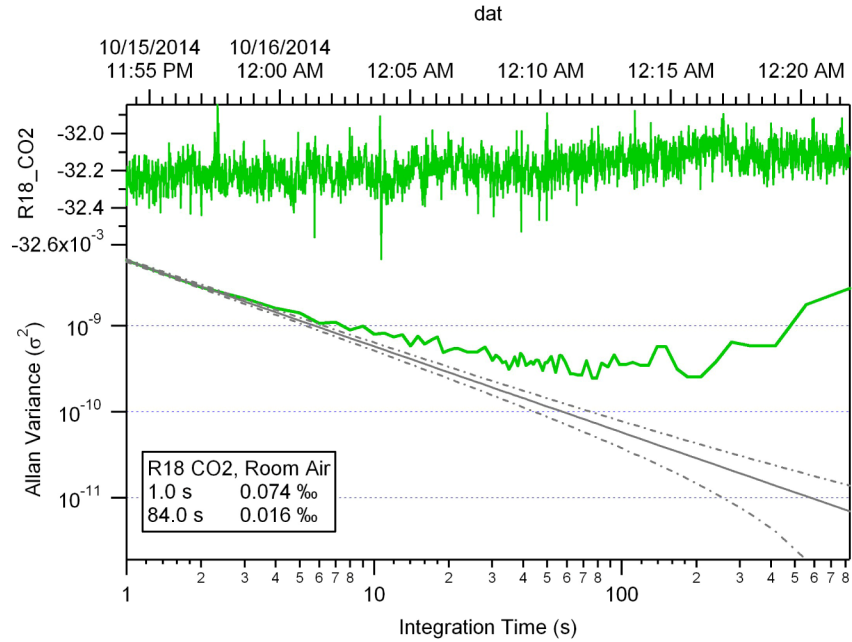


Fig. 4. Allan-Werle plot, variance vs. integration time, for isotopologue ratio  $^{12}\text{C}^{18}\text{O}^{16}\text{O}/^{12}\text{C}^{16}\text{O}_2$ , ambient air sample.

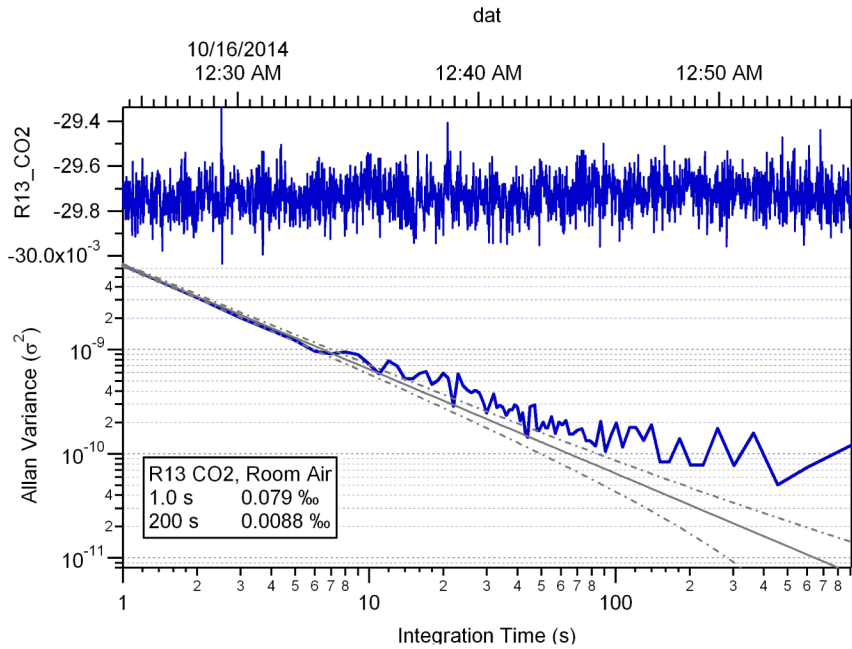


Fig. 5. Allan-Werle plot, variance vs. integration time, for isotopologue ratio  $^{13}\text{C}^{16}\text{O}_2/^{12}\text{C}^{16}\text{O}_2$ , ambient air sample.

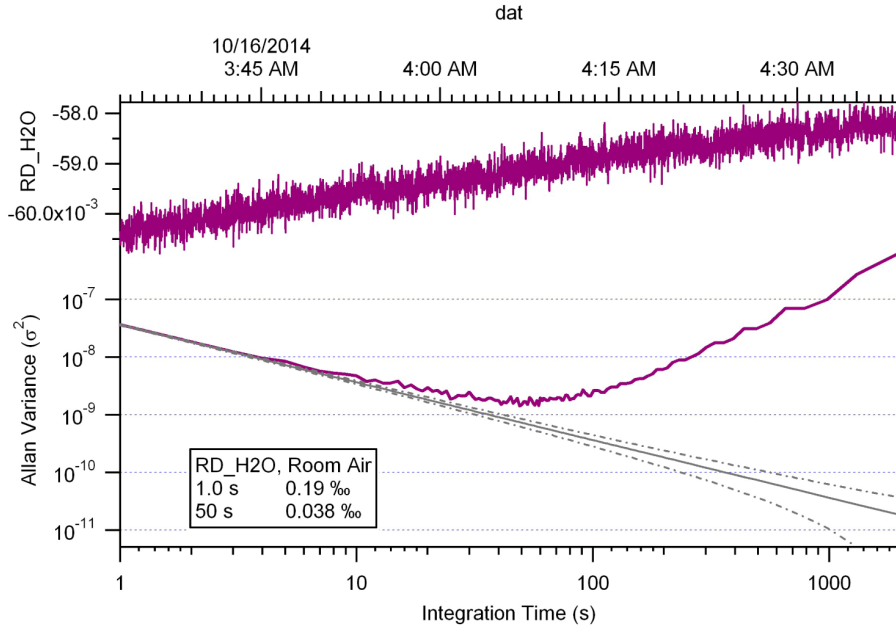


Fig. 6. Allan-Werle plot, variance vs. integration time, for isotopologue ratio  $[HDO]/[H_2O]$ , ambient air sample.

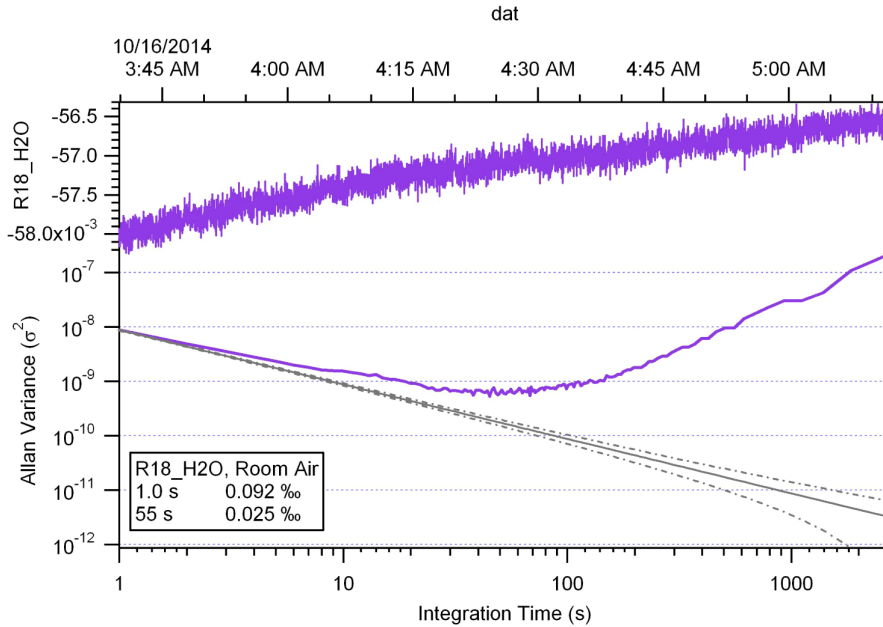


Fig. 7. Allan-Werle plot, variance vs. integration time, for isotopologue ratio  $[H_2^{18}O]/[H_2O]$ , ambient air sample.

#### 4.2 Tests of the calibration system

We have tested the instrument with a prototype dual dilution calibration system of the configuration shown in Fig. 3. In our implementation, the concentration ranges that are delivered can be controlled by the timing of valves that are opened by the instrument computer, as well as by the temperature of the “standard” water reservoir and by the pressure

of the  $\text{CO}_2$  in the storage tube. By flowing dry  $\text{CO}_2$ -free air through the calibration system, measurement offsets from zero can be determined and subtracted. Isotopic ratios are formed from the adjusted mixing ratios. Fourth-order polynomial fits of isotopic ratio versus concentration are done for the dilution periods. The fit parameters are interpolated between calibration periods to make a function of ratio versus concentration for the local standard that is continuous through the sample periods. The sample isotopic ratios then are divided by the extrapolated standard ratios, at matching concentrations. Thus, a first isotopic super-ratio ( $\mathbf{R}$ ) is formed. The super-ratio can then be shifted according to a calibration that compares the local standard to a global standard. Since the deviation in isotopic content of natural samples is small,  $\mathbf{R} \approx 1$ . The literature on isotopic measurements often reports the deviation from  $\mathbf{R} = 1$  as “delta”,  $\delta = (\mathbf{R}-1) \times 1000$ .

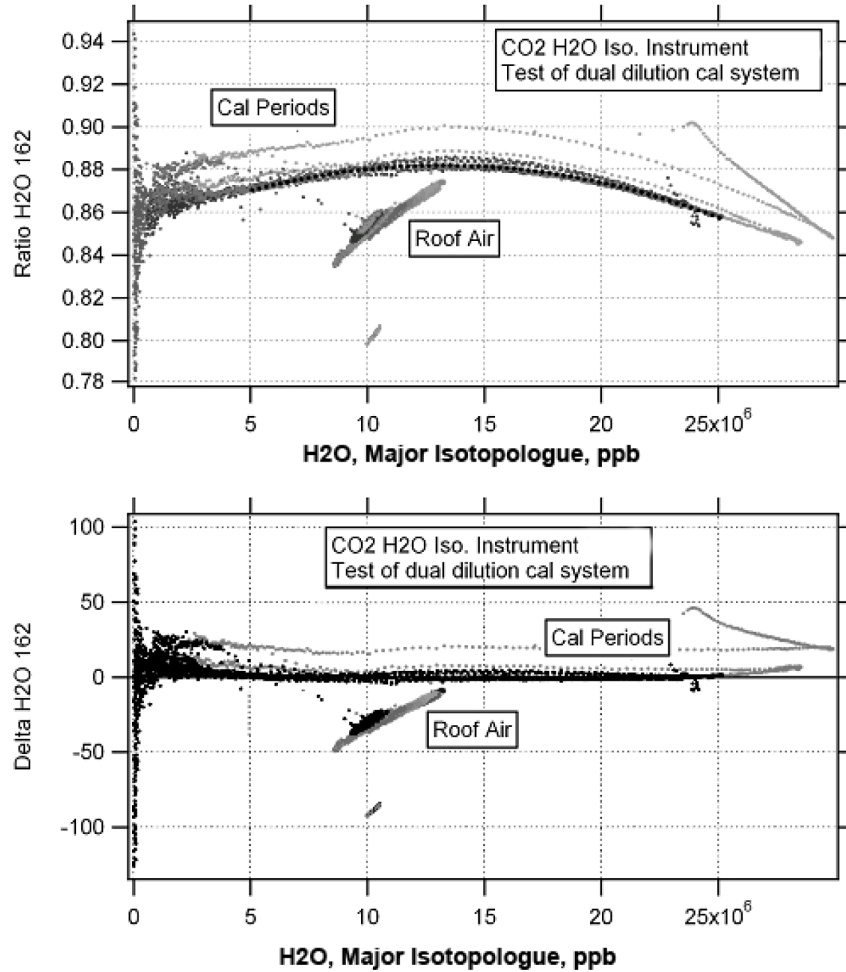


Fig. 8. Examples of the application of the interpolated polynomial fit method for the isotopic ratio for deuterated water,  $\text{HDO}/\text{H}_2\text{O}$ , for rooftop ambient sampling data. The Hitran [32] isotopic designation is used in the axis labels, so that “162” refers to  $^1\text{H}^{16}\text{O}^2\text{H}$ . “Delta H2O 162” =  $(\{ [^1\text{H}^{16}\text{O}^2\text{H}]/[^1\text{H}_2^{16}\text{O}] \}_{\text{sample}} / \{ [^1\text{H}^{16}\text{O}^2\text{H}]/[^1\text{H}_2^{16}\text{O}] \}_{\text{ref. mtl}} - 1) \times 1000$ , and [\*] indicates concentration. The calibration periods are the sets of points that span a wide concentration range. The upper panel shows concentration dependence in the measurement of a given standard material, but the calibration algorithm compensates for that dependence. The resulting atmospheric deltas then should be more accurate.

Examples of the application of the interpolated polynomial fit calibration are shown in Figs. 8 and 9. Each figure is an arrangement of two plots, based on data collected over four days of sampling rooftop air. Each image shows isotopic ratio or delta versus CO<sub>2</sub> concentration, with two plots each for CO<sub>2</sub> (<sup>13</sup>C) and for H<sub>2</sub>O (HDO). The top plots of each pair are ratios of concentrations ([minor isotopologue]/[major isotopologue]) before calibration has been applied, and the bottom plots are after calibration corrections have been applied. The calibration period points extend across a wide range of concentration, and the rooftop sampling points are a cluster over a narrower range of concentration. There is a clear concentration-dependence of the isotopologue ratios. After calibration adjustment, the calibration-period points fall on a straight line. The reasons for the concentration dependence continue to be a matter of inquiry.

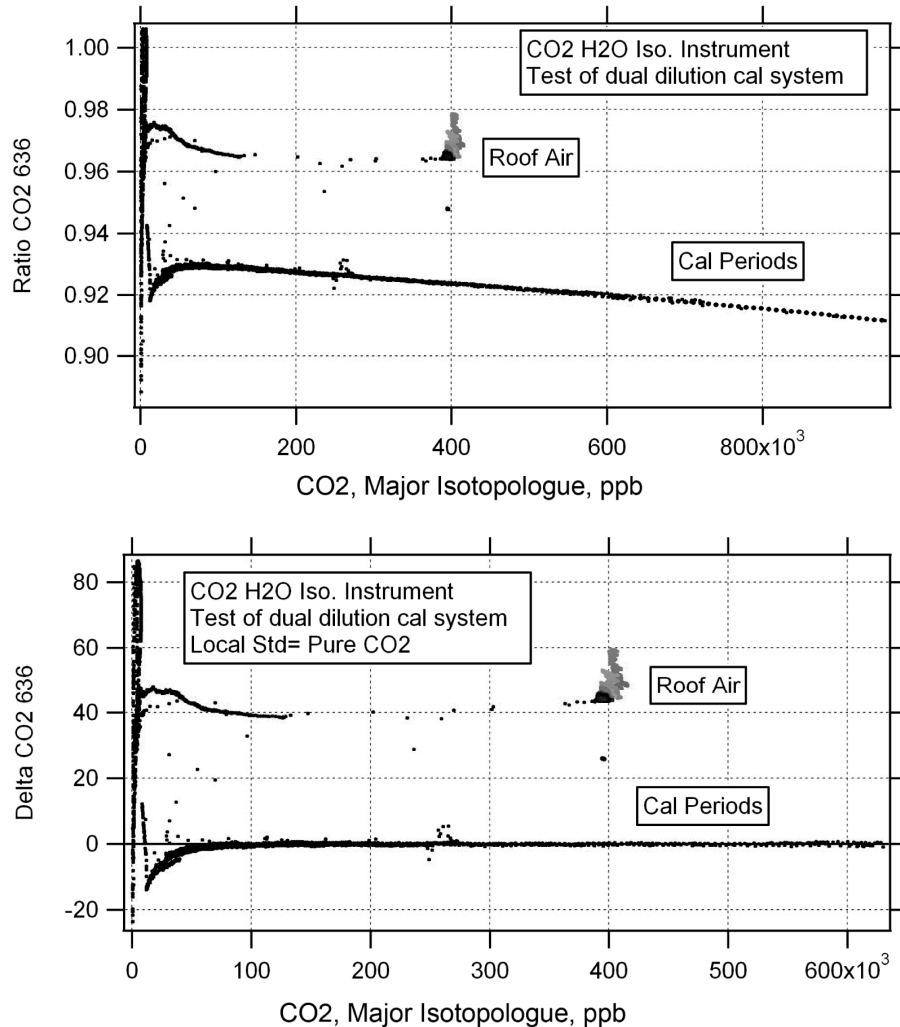


Fig. 9. Examples of the application of the interpolated polynomial fit method for isotopic ratio <sup>13</sup>CO<sub>2</sub>/<sup>12</sup>CO<sub>2</sub> for rooftop ambient sampling data. The Hitran [32] isotopic designation is used in the axis labels, so that “636” refers to <sup>16</sup>O<sup>13</sup>C<sup>16</sup>O. “Delta CO2 626” = ( $\frac{[^{16}\text{O}^{13}\text{C}^{16}\text{O}]}{[^{12}\text{C}^{16}\text{O}_2]}\bigg|_{\text{sample}} / \frac{[^{16}\text{O}^{13}\text{C}^{16}\text{O}]}{[^{12}\text{C}^{16}\text{O}_2]}\bigg|_{\text{ref. mtl}} - 1$ ) x 1000, and [\*] indicates concentration. The calibration periods are the sets of points that span a wide concentration range. The upper panel shows concentration dependence in the measurement of a given standard material, but the calibration algorithm compensates for that dependence. The resulting atmospheric deltas then should be more accurate.

## 5. Analysis of instrument noise

While the instrument noise performance described above is rather good, we would like to understand the sources of noise and drift so that better performance may be achieved in the future. The Allan-Werle plots presented above show the instrument noise and drift, but do not provide many clues as to the causes of those performance limits. Other analytical tools may be applied to better understand the effects limiting performance.

Partitioning measurement noise by type can help to indicate its origin. Three frequently used practical noise categories are: “dark”, “light” and “proportional”. “Dark noise”, (i.e. mixing ratio reported with detector blocked) includes: detector noise, fundamental electronic (Johnson) noise, and possibly excess electronic noise. “Light noise” (normal light levels but very small absorption depths, i.e. with dry CO<sub>2</sub> free “zero-air” sample) includes all the dark noise plus: laser noise (1/f, i.e. flicker, and shot), laser drive current noise (producing amplitude fluctuations), and variation in interference fringes. “Proportional noise” (excess noise seen when the absorption depth is greater) includes: laser drive current noise (producing frequency modulation), and peak position motion combined with tuning rate errors. Such a noise partition is presented in Table 3, for the individual isotopologues (in terms of the concentration and in terms of the optical depth, OD, for each absorption line). OD's are the line optical depths (-ln(Transmission)), given for typical ambient concentrations. OD/ppb is the line depth per unit concentration. Noise for three sample types are given: “Amb.” = ambient air; with deep absorption lines showing “proportional noise”; “Zero air” is dry, CO<sub>2</sub> free air giving no absorption lines, i.e. showing “light noise”; and “Dark” is with the detector blocked, showing “dark” noise. Columns labeled “ppb” are concentration noise. OD noise is calculated as: (mixing ratio noise, ppb)\*(specific line depth, OD/ppb). Dark noise is calculated in terms of the light level that is normally present.

The data in Table 3 provides some initial clues on the sources of noise in the instrument. The dark noise, when expressed as a signal voltage, is nearly constant at  $\sim 9 \times 10^{-3}$  mV. The light noise is approximately twice the dark noise, for both lasers. The instrument has excess proportional noise, several times the light noise for the deeper lines. The ratio of: (Proportional noise)/(Optical depth), is nearly constant at  $\sim 6 \times 10^{-5}$ . Thus, the proportional noise has the greatest impact on the measurement.

**Table 3. Noise partition results for H<sub>2</sub>O-CO<sub>2</sub> isotope instrument, 1s averages**

Gas	OD	Amb.			Zero			Dark		
		σ, ppb			σ, ppb			σ, ppb		
		OD/ppb								
H <sub>2</sub> O	2.35	1.8x10 <sup>-7</sup>	980	170	77	1.8x10 <sup>-4</sup>	3.2x10 <sup>-5</sup>	1.4x10 <sup>-5</sup>		
HDO	0.039	3.3x10 <sup>-9</sup>	2400	2700	2050	7.8x10 <sup>-6</sup>	8.8x10 <sup>-6</sup>	6.7x10 <sup>-6</sup>		
H <sub>2</sub> <sup>18</sup> O	0.20	1.6x10 <sup>-8</sup>	1240	1240	600	2.0x10 <sup>-5</sup>	1.3x10 <sup>-5</sup>	9.8x10 <sup>-6</sup>		
CO <sub>2</sub>	0.83	1.6x10 <sup>-6</sup>	24.5	3.0	1.5	3.8x10 <sup>-5</sup>	4.7x10 <sup>-6</sup>	2.3x10 <sup>-6</sup>		
C <sup>17</sup> OO	0.1	1.2x10 <sup>-7</sup>	72	29	14	8.6x10 <sup>-6</sup>	3.5x10 <sup>-6</sup>	1.7x10 <sup>-6</sup>		
C <sup>18</sup> OO	0.81	1.6x10 <sup>-6</sup>	27	3.0	1.7	4.2x10 <sup>-5</sup>	4.7x10 <sup>-6</sup>	2.7x10 <sup>-6</sup>		
<sup>13</sup> CO <sub>2</sub>	1.17	2.3x10 <sup>-6</sup>	27	2.8	1.3	6.2x10 <sup>-5</sup>	6.4x10 <sup>-6</sup>	3.0x10 <sup>-6</sup>		

“Amb” refers to ambient concentration of the gas, “Zero” is air without any of the gas, and “Dark” is a measurement with the detector blocked. Noise is presented in terms of concentration (ppb) and optical depth (OD).

There are several other analytical techniques that can help characterize excess noise, especially when applied to sets of spectra that have been recorded without averaging, at the sweep rate of  $\sim 1$ -3 kHz. It also is convenient to organize the data sets into arrays, where individual spectra are vertically stacked rows in the array. We have presented these concepts in more detail in a recently submitted paper [40]. A simple test for proportional noise is to examine the channel-dependent noise in the spectra. In this test we first normalize the spectra by averages of the rows, to remove simple sweep-to-sweep amplitude variations. Then we

subtract the average spectral shape (shown in red in Fig. 10) to reveal small fluctuations across the spectra. We calculate the standard deviation for each column in the resulting spectral array to arrive at the noise for each channel (shown as the blue trace in Fig. 10). In this case, there are strong enhancements of noise in the channels where there are deep absorption lines, which is an indication of unwanted frequency-modulation (FM) by a stray electrical signal entering the laser driver. High frequency current modulation generally will produce amplitude-modulation (AM) as well as FM. FM produces an amplitude signal that is sensitive to the derivative of the light signal with respect to the frequency scale ( $\nu$ ), i.e. given a spectrum,  $I(\nu)$  subject to small frequency perturbations,  $\Delta$ , the perturbed intensity is approximately  $I(\nu + \Delta) \approx \Delta \frac{dI(\nu)}{d\nu}$ . The light fluctuations, in terms of variance are expressed as:  $\sigma^2(I) \approx \sigma^2(\Delta) \left(\frac{dI(\nu)}{d\nu}\right)^2$ . When we plot spectral shape in terms of channels ( $c$ ) we need to include the variable laser tuning rate,  $d\nu/dc$ , as:  $\frac{dI(\nu)}{d\nu} = \left(\frac{dI(c)/dc}{d\nu/dc}\right)$ . The magnitude of the FM thus can be estimated by finding the slope when plotting the channel variance in the spectrum as a function of the square of the spectral slope, as shown in Fig. 11. This analysis method also illustrates how FM can be a somewhat hidden form of noise, barely noticeable in the spectral regions without much absorption, but dominant just where it matters, at the absorption lines.

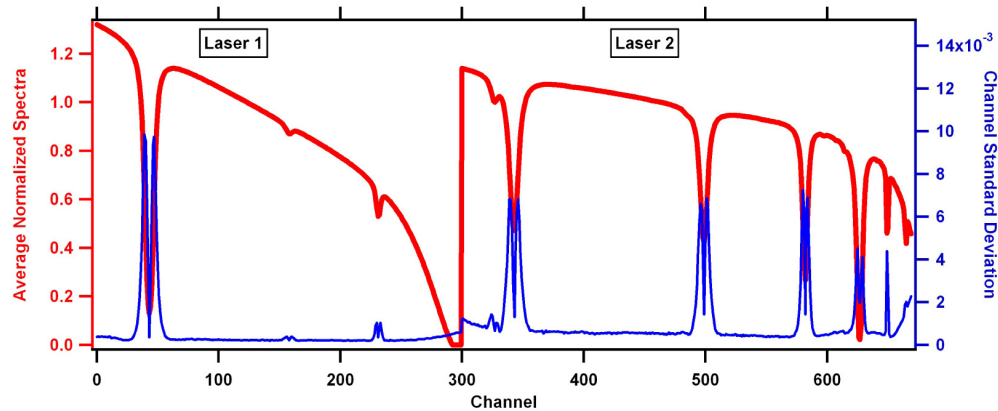


Fig. 10. Average normalized spectra for both lasers (red trace), and noise in each channel (standard deviation) (blue trace). The higher channel noise at the sides of the absorption lines indicates laser frequency modulation.

Different types of Fourier transforms help us to identify the specific frequencies producing the unwanted FM. If we do Fourier transforms (power spectra) on the columns (channels) in the spectral array, then we can observe increased noise power at the positions of deep absorption lines, as shown in Fig. 12. For the laser 2 section of Fig. 12 there is further enhancement of noise power at the specific per-sweep frequency of 0.3. In this case the sampling rate is 1538 kHz and each laser sweep has 750 channels (300 channels for laser 1, 400 channels for laser 2, and 50 channels with both lasers off). The sweep frequency then is 2.05 kHz ( $1538/750$ ), and the 0.3 per-sweep frequency of the enhanced noise power is would appear at 615 Hz. That frequency provides a clue to the source of the FM, but additional information is needed.

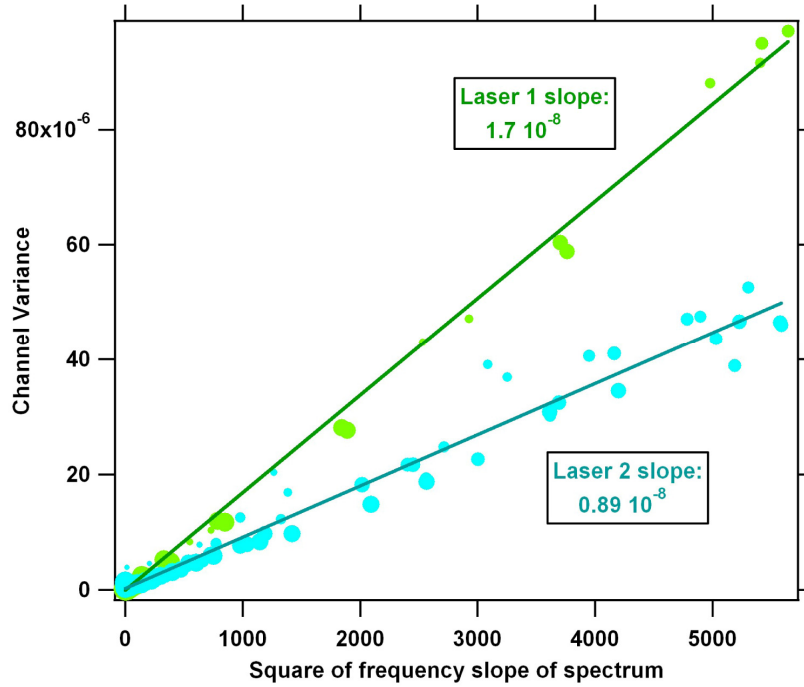


Fig. 11. The plot above shows channel variance plotted against the square of the derivative of the average spectrum versus frequency. The plot quantifies the frequency modulation for both lasers, as the slope is expected to be the variance in the frequency. This gives the standard deviations of the frequency modulation (square roots of the slopes) as  $1.3 \times 10^{-4} \text{ cm}^{-1}$  for laser 1, and  $0.9 \times 10^{-4} \text{ cm}^{-1}$  for laser 2. That amount of frequency modulation corresponds to  $\sim 1/10$  of a measurement channel.

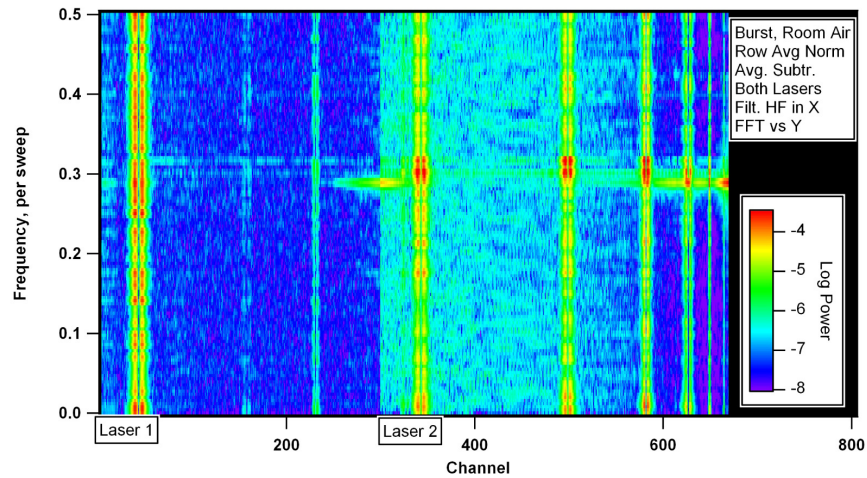


Fig. 12. FFT (power spectra) of columns in the spectral array recorded without averaging. The false color represents the log of the power density. There is diffuse noise distributed across the spectra, as well as vertical stripes of increased noise power at the (channel) locations of the deep absorption lines (appearing yellow to red). Further enhanced noise power is seen at per-sweep frequency. For laser 2 the Y-frequency is clearly  $\sim 0.3$ , which matches the Y-frequency seen in the zero-air burst. The matching X-frequency then was 0.251 per channel, the 380 kHz switching frequency. The Y-frequency for laser 1 is less clear.

A two-dimensional power spectrum provides a link between per-channel periodicities and per-sweep periodicities stemming from the same cause. The link between can be understood by considering an array of spectra,  $[S(c, r)]$ , signal vs channel ( $c$ ) and row ( $r$ ) containing a single high frequency ( $f_e$ ) electronic signal,  $E(t) = E_o \sin(2\pi f_e t)$ . Then, with sampling rate  $F_{AD}$  and samples per scan,  $N_s$ , the sweep frequency is  $F_s = F_{AD} / N_s$ , and time and signal in the array are:

$$t(c, r) = c / F_s + r N_s / F_{AD} \quad \text{Eq. (2)}$$

$$S(c, r) = E_o \sin[2\pi c f_e / F_s + 2\pi r f_e N_s / F_{AD}] = E_o \sin[2\pi c f_e / F_s + 2\pi r f_e / F_s] \quad \text{Eq. (3)}$$

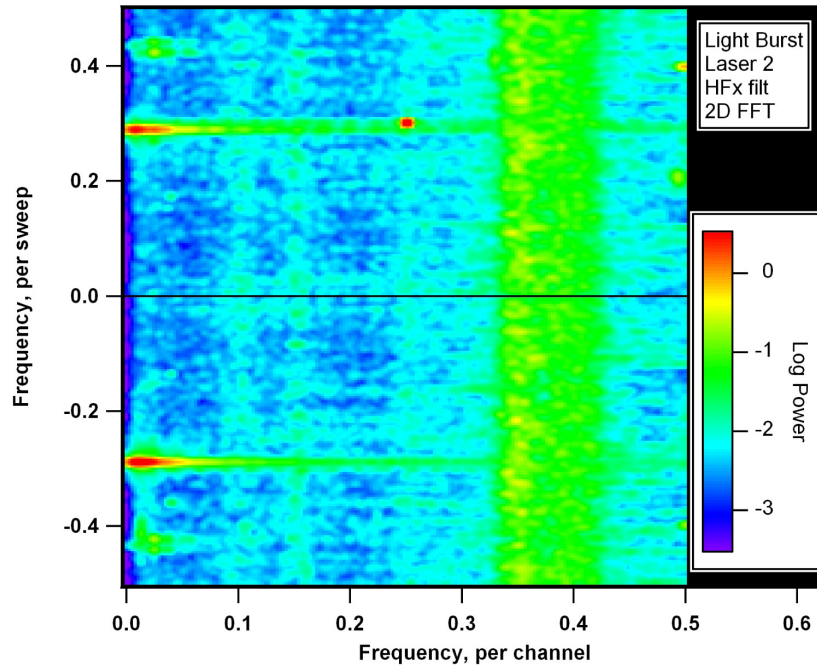


Fig. 13. 2D-FFT of the laser 2 signal recorded without averaging, at 2 kHz. The false color represents the log of the power density. Here the normalized average-subtracted array has been filtered to remove low frequency fluctuations. There is a power spike at  $(f_x, f_y) = [0.25, 0.30]$  due to frequency modulation. The x-frequency (0.25 per channel) corresponds to an electrical frequency of  $\sim 380$  kHz, which is the power supply switching frequency. The power spikes at  $[<0.05, \pm 0.30]$  are due to the same FM acting on the absorption line-shapes.

In most cases that we encounter,  $f_e \gg F_s$ , i.e. the electronic signal may be well beyond the Nyquist sampling limit for the sweep frequency and the electronic signal will be aliased so as appear at a much lower per-sweep frequency. The 0.3 per-sweep frequency of the enhanced noise power seen in Fig. 12 is such an alias, so that the observed periodicity is not meaningful by itself, except that in a 2-D power spectrum the per-sweep frequency is linked to the corresponding per-channel frequency, which may not be aliased. A 2-D power spectrum for our un-averaged spectral array is shown in Fig. 13, and we do see a power density spike at the per-channel frequency 0.25 (horizontal axis) and the per-sweep frequency 0.3 (vertical axis), described in the caption of Fig. 13 as:  $[f_x = 0.25, f_y = 0.3]$ . If un-aliased, the per-channel frequency 0.25 corresponds to  $\sim 380$  kHz, which is the frequency of our DC-DC conversion power supply master switching frequency. Our switching power supply frequency has been designed to be highly stable so that we can recognize its influence in the spectra, as we do here. In Fig. 13 we also see two other power spikes, at the same per-sweep frequency ( $\pm 0.3$ ) but at low per-channel frequency ( $<0.05$ ). Those two other noise spikes are actually due to

FM at the absorption line positions, while the noise spike at [ $f_x = 0.25$ ,  $f_y = 0.3$ ] is due to FM acting on the sloping spectral baseline. The wide vertical stripe of noise power near 0.38 per-channel is due to an interference fringe with a generating length of 278 cm, originating in the path between the laser and the back mirror of the absorption cell. The feature is wide in frequency because the fringe is a pure frequency on the non-linear laser tuning scale, while the Fourier transform (FFT) assumes a uniform frequency spacing. When we do a Fourier analysis that takes into account the non-linear laser tuning (a Lomb power spectrum), interference fringe features will be sharp, while electronic features become blurred. In fact, that difference in appearance between FFT power spectra and Lomb power spectra can help to distinguish between interference fringes and electronic signals in laser spectra.

## 6. Conclusions

In this paper we have reviewed our general instrument design approaches, which often result in measurements with absorption noise of  $\sim 5 \times 10^{-6}$  with a 1s average. We have presented the design of a new two-laser instrument for simultaneous measurement (in a single 36 m multi-pass cell) of seven isotopologues of carbon dioxide and water vapor. The instrument employs a QCL operating at  $2310 \text{ cm}^{-1}$  ( $4.3 \text{ }\mu\text{m}$ ) and an antimonide TDL operating at  $3765 \text{ cm}^{-1}$  ( $2.77 \text{ }\mu\text{m}$ ). Isotope ratios for  $^{13}\text{CO}_2$  and  $\text{C}^{18}\text{O}^{16}\text{O}$  are measured with a precision of approximately 0.1‰ in 1s. Isotope ratios for HDO and  $\text{H}_2^{18}\text{O}$  are measured with precisions of 0.3‰ and 0.1‰ in 1s, respectively. We have also presented a design for a calibration system that covers a wide range of concentrations so that instrument nonlinearities are compensated.

We have presented a noise analysis for the carbon dioxide and water vapor isotope instrument, in order to determine the source of excess “proportional” noise at the level of  $5 \times 10^{-6}$  absorption. We find that our main power-supply switching frequency is the source of frequency-modulation that produces excess noise. The analysis pathways presented are a small subset of the many methods we have explored in the process of careful evaluation of more than 100 commercial instruments. In future work we plan to more comprehensively describe those analysis methods.

## Acknowledgments

We are grateful to our other team members at Aerodyne Research, Inc., Joanne Shorter, Scott Hearndon, Rob Roscioli, Tara Yacovitch, Dylan Jarvis, Mike Agnese, Ryan McGovern, Stanley Huang and Mike Moore. We also gratefully acknowledge the financial support of the SBIR program at the US Department of Energy.